5 3D FEL analysis

Chapter 5 extends the one-dimensional (1D) theoretical analysis of FELs to the three-dimensional (3D) regime. Although the FEL interaction is predominantly longitudinal in nature, transverse physics cannot be neglected if one wants to have a complete picture of the FEL. Specifically, we must understand the roles of radiation diffraction and guiding, and the how the electron beam emittance and betatron motion in the undulator affect performance. We first describe these effects qualitatively in Sec. 5.1, where we emphasize the underlying physical picture. In Sec. 5.2 we revisit the electron trajectory in the undulator, taking into account the 3D undulator magnetic field and the coupling of the transverse degrees of freedom to the longitudinal motion. Section 5.3 generalizes the FEL pendulum equations and the 1D field equation to 3D by including these transverse effects. The low-gain solution will be presented in Sec. 5.4 in the form of a generalized Madey theorem. To solve the coupled Maxwell-Klimotovich equations in the high-gain regime, Van Kampen's normal mode expansion is introduced in Sec. 5.5, and a 3D dispersion relation is derived for the radiation growth rate in terms of four universal scaled parameters. Finally, a powerful variational solution is discussed and a handy fitting formula for the FEL gain length is presented near the end of this chapter.

5.1 Qualitative Discussion

5.1.1 Diffraction and Guiding

A remarkable feature of a SASE FEL is its transverse coherence. As we have discussed, the spontaneous undulator radiation has a transverse phase space area that is determined by the electron beam emittance $(2\pi\varepsilon_x)^2$. This area is typically much larger than the diffraction-limited phase space area $(\lambda/2)^2$, especially at x-ray wavelengths, so that undulator radiation is composed of many transverse modes. In a SASE FEL, the initial transverse phase space of the spontaneous emission also consists of an incoherent sum of many spatial modes. However, since the FEL interaction is localized within the electron beam near the peak electron density, there is one "dominant" mode whose transverse size σ_r is dictated by the beam area, and whose natural divergence satisfies $\sigma_r\sigma_{r'} = \lambda/4\pi$. Higher order spatial modes either diffract more, which results in greater effective

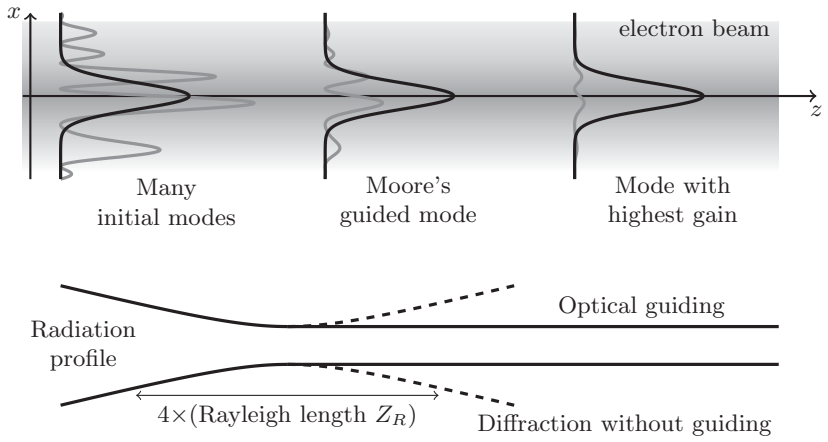

Figure 5.1 Illustration of Moore's guided mode. In the top panel the preferentially guided mode is plotted in black, while the higher order modes are in gray. The intensity at each z location is scaled to keep the height of the guided (black) mode invariant, so that what appears to be a decrease in the power in the higher order (gray) modes is actually the larger gain of the Gaussian guided profile outstripping the smaller gain associated with all other modes. The bottom panel compares the natural diffraction of the radiation with that of the guided mode generated by FEL gain.

losses, or are of larger spatial extent and couple less efficiently to the particles. Thus, the fundamental mode has the highest effective gain, so that it eventually becomes the preferred spatial distribution for the SASE radiation. This surviving fundamental mode appears to be guided after a sufficient undulator distance, a phenomenon commonly referred to as "optical guiding" or "gain guiding" [1, 2].

We illustrate the general idea of gain guiding schematically in Fig. 5.1. The initial radiation is assumed to have a broad distribution of many transverse modes. Since gain is only effective within the central area, however, one "matched" transverse mode shape is selected over all others, and this mode then appears to be guided over many vacuum Rayleigh lengths due to the gain. The transverse mode selection is also clearly evident in Fig. 5.2, which was obtained from a 3D GENESIS simulation of SASE. Initially, the radiation power is randomly distributed in the transverse plane, but after a sufficient amount of propagation only one localized coherent mode survives. Note that in order for one Gaussian-like transverse mode to completely dominate, there must be enough propagation time for the competing modes to communicate transversely via diffraction.

In the 1D analysis, we introduced the important FEL scaling or Pierce parameter ρ, defined through the relation $n_e\kappa_1\chi_1 = 4k_u^2\rho^3$ which is equivalent to

$$\rho = \left(\frac{e^2K^2[\mathrm{JJ}]^2n_e}{32\epsilon_0\gamma_r^3mc^2k_u^2}\right)^{1/3} = \left[\frac{1}{8\pi}\frac{I}{I_A}\left(\frac{K[\mathrm{JJ}]}{1+K^2/2}\right)^2\frac{\gamma_r\lambda_1^2}{2\pi\sigma_x^2}\right]^{1/3}, \qquad (5.1)$$

where $I_A = ec/r_e \approx 17045$ A is the Alfvén current. Many important charac-

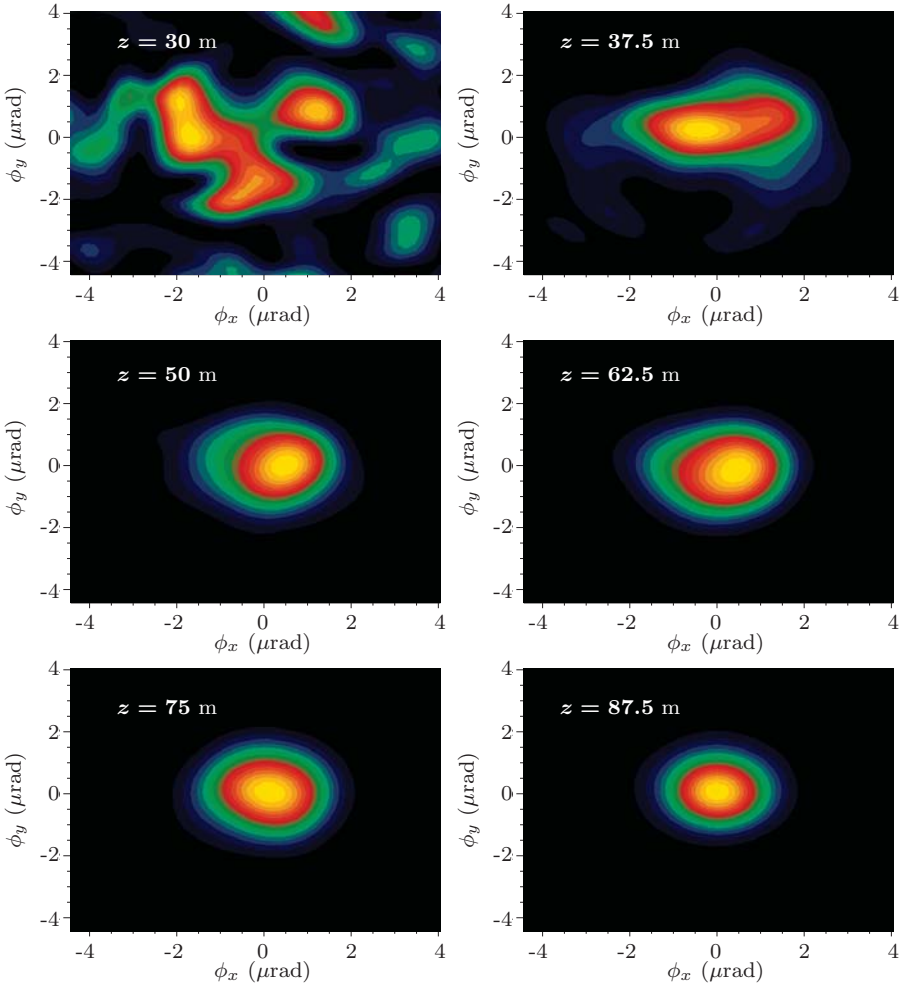

Figure 5.2 Evolution of the LCLS radiation angular distribution at different z location. Courtesy of S. Reiche.

teristics of the FEL scale with ρ: the gain length and saturation length scale inversely with ρ, while the bandwidth is proportional to ρ. To be more explicit, for vanishing e-beam energy spread the ideal gain length is given by

$$L_{G0} = \frac{\lambda_u}{4\sqrt{3}\pi\rho}. \tag{5.2}$$

When 3D effects are included, a different dimensionless combination of parameters may govern the gain characteristics of the FEL. To see this, consider the extreme case where the effect of diffraction is "large," meaning that the radiation mode size is significantly larger than the electron beam size. To better describe the interaction between the electrons and the radiation in this 3D limit,

the beam area $2\pi\sigma_x^2$ in Eq. (5.1) should be replaced by the diffraction limited cross section introduced in Ch. 1.2.1, i.e.,

$$2\pi\sigma_x^2 \;\rightarrow\; 2\pi\frac{\lambda_1}{4\pi}Z_R. \tag{5.3}$$

Here Z_R is the Rayleigh length of the radiation, which from our discussion on gain guiding ought to be of order a few gain lengths. Thus, by inserting $2\pi\sigma_x^2 \rightarrow \lambda_1 L_G$ into Eq. (5.1) and then the resulting expression for ρ into (5.2), one can solve the resulting algebraic equation for the gain length L_G to find

$$L_G^{-1} = \frac{4\pi}{\lambda_u}\frac{3^{3/4}}{2}\sqrt{\frac{I}{\gamma I_A}\frac{K^2[\mathrm{JJ}]^2}{(1+K^2/2)}}. \tag{5.4}$$

This equation gives an approximate formula for the growth rate when the 3D effect of diffraction dominates, specifically, when the optical mode is larger than the electron beam cross sectional area. Thus, it may be convenient to introduce the diffraction D-scaling for certain FEL applications as was done in Ref. [3]. Notice that L_G^{-1} scales as $I^{1/2}$ in the 3D diffractive limit, which is in contrast to the $I^{1/3}$ behavior that characterizes the 1D limit when the electron beam size is larger than that of the optical mode. Additionally, the D-scaling shows that shrinking the electron beam cross section much below that of the radiation mode does not further reduce the gain length. In fact, reducing the beam size beyond a certain point actually tends to increase the gain length, since decreasing the physical beam size necessarily increases the angular spread of an electron beam with non-zero emittance. While we will investigate the e-beam and radiation divergence further in the next section, it is evident from this discussion that the optimal electron beam size should roughly match the size of the radiation beam:

$$\sigma_x \sim \sigma_r = \sqrt{\varepsilon_r Z_R} \sim \sqrt{\varepsilon_r L_G}, \tag{5.5}$$

where $\varepsilon_r = \lambda_1/4\pi$ is the radiation emittance.

The above qualitative arguments are useful for understanding the effect of diffraction and for estimating the gain length of certain high-gain FEL projects operating in the infra-red and visible wavelengths, where the optical mode size is larger than the e-beam size. Nevertheless, we will continue to scale quantities by the dimensionless parameter ρ for two reasons. First, ρ-scaling is more relevant for x-ray FELs because the typical optical mode size is smaller than the rms beam size. Second, ρ does not require introducing the (formally undetermined) Rayleigh range, and instead relies on the electron beam cross sectional area:

$$\rho = \frac{1}{2\gamma_r}\left[\frac{I}{I_A}\left(\frac{\lambda_u K[\mathrm{JJ}]}{\sqrt{2}2\pi\sigma_x}\right)^2\right]^{1/3}. \tag{5.6}$$

5.1.2 Beam Emittance and Focusing

An electron beam with finite emittance ε_x has a rms angular spread $\sigma_{x'} = \varepsilon_x/\sigma_x$, so that its size will expand in free space as we discussed in Ch. 1.1.4 and ex-

pressed in Eq. (1.26). Hence, to keep a nearly constant e-beam size and maximize the FEL interaction in a long undulator channel requires proper electron focusing. As shown in the next section, the undulator magnetic field does provide a "natural" focusing effect. The natural focusing strength, however, is typically too weak, so that external focusing by quadrupole magnets is often required. This focusing is used to decrease the beam size, thereby increasing the ρ parameter and decreasing the gain length. As mentioned in the previous section, decreasing the beam size below that of the optical mode may actually degrade the FEL performance, because the increasing angular spread introduces a spread in the resonant wavelength. This effect is similar to that of energy spread, and can be understood by considering the FEL resonance condition

$$\lambda_1(\psi) = \frac{\lambda_u}{2\gamma^2}\left(1 + \frac{K^2}{2} + \gamma^2\psi^2\right), \tag{5.7}$$

where ψ is the angle the particle trajectory[1] makes with respect to the z-axis. From Eq. (5.7), we see that the spread in particle angles given by $\Delta\psi = \sigma_{x'}$ causes a spread in the resonant wavelength

$$\frac{\Delta\lambda}{\lambda_1} = \sigma_{x'}^2\frac{\lambda_u}{\lambda_1} = \frac{\varepsilon_x}{\beta_x}\frac{\lambda_u}{\lambda_1}. \tag{5.8}$$

To not adversely affect the FEL gain, we demand that the induced wavelength variation due to the angular spread be less than the FEL bandwidth $\sim \rho$, namely that

$$\frac{\Delta\lambda}{\lambda_1} = \sigma_{x'}^2\frac{\lambda_u}{\lambda_1} \lesssim \rho \approx \frac{\lambda_u}{4\pi L_G}. \tag{5.9}$$

Due to optical guiding, the radiation Rayleigh range is of order the gain length, $Z_R \sim L_G$, so that (5.9) implies that the electron beam angular divergence should be no more than that of the radiation:

$$\sigma_{x'} = \sqrt{\frac{\varepsilon_x}{\beta_x}} \leq \sqrt{\frac{\varepsilon_r}{L_G}} \sim \sigma_{r'}. \tag{5.10}$$

The inequalities regarding the beam size (5.5) and angular divergence (5.10) together require

$$\varepsilon_{x,y} \lesssim \varepsilon_r = \frac{\lambda_1}{4\pi}, \tag{5.11}$$

while the optimal focusing beta function for a given emittance saturates the inequality (5.10):

$$\beta_x \sim L_G\frac{\varepsilon_x}{\varepsilon_r}. \tag{5.12}$$

A smaller beam emittance allows for a tighter focused beam size, and hence a smaller gain length. In the following sections, we expand upon these qualitative arguments by quantitatively studying the effects of diffraction, guiding, beam emittance, and betatron motion on the FEL gain.

[1] We found essentially the same formula in Eq (2.49) in terms of the optical angle ϕ, since one can exchange $\phi \leftrightarrow \psi$ by redefining the optical axis.

5.2 Electron Trajectory

In the previous chapter on 1D FEL theory, we considered motion in the undulator field

$$\boldsymbol{B}(0,0,z) = -B_0 \sin(k_u z)\hat{y}, \tag{5.13}$$

and showed that the electron trajectory in the transverse plane was given by the "wiggle motion"

$$x_w(z) = \frac{K}{\gamma k_u}\sin(k_u z) \qquad\qquad y_w(z) = 0, \tag{5.14}$$

where $K \equiv eB_0/mck_u$ is the dimensionless deflection (or undulator) parameter. Equation (5.14) represents the ideal trajectory of an electron injected along the optical axis of the undulator. Our description of the full transverse dynamics associated with arbitrary initial conditions will average over the fast oscillations in the undulator field in a manner similar to that of the previous chapter. There, the averaged equations described the slowly evolving longitudinal coordinates (θ, η); in this chapter, we will include the transverse degrees of freedom, paying particular attention to the variation in phase θ caused by non-zero $(\boldsymbol{x}, \boldsymbol{p})$. We write the transverse coordinates as a sum of the wiggle motion and the slow (betatron) evolution:

$$x(z) = x_w(z) + x_\beta(z), \tag{5.15}$$

$$y(z) = y_\beta(z). \tag{5.16}$$

In Eqs. (5.15)-(5.16), $\boldsymbol{x}_\beta(z)$ is the slowly evolving part of $\boldsymbol{x}$ that represents the transverse beam envelope. If the magnetic field (5.13) described an actual undulator, for example, than $\boldsymbol{x}_\beta(z) = \boldsymbol{x}(0) + \boldsymbol{x}'(0)z$, and the transverse dynamics would be simple rectilinear motion[2]. Realizable undulator fields, however, focus the electrons transversely which results in a slow oscillatory motion whose period is much longer than the undulator wavelength λ_u. The combined fast (wiggle) and slow (betatron) motion is shown in Fig. 5.3.

In general, the amplitude of the betatron oscillation is larger than that of the undulator wiggle motion. To determine the betatron motion more precisely, we must investigate the magnetic field at points other than those along the z-axis.

5.2.1 Natural Focusing in an Undulator

The undulator field Eq. (5.13) is only valid very near the $y = 0$ plane because it does not satisfy the vacuum Maxwell equations in 3D [i.e., the curl of Eq. (5.13) does not vanish]. An exact solution of Maxwell's equations describing a planar

[2] This is the transverse motion we used in Ch. 2.4 to study undulator radiation. It is an appropriate approximation if the undulator length L_u is much shorter than the natural undulator focusing length $\sim \gamma\lambda_u/K$.

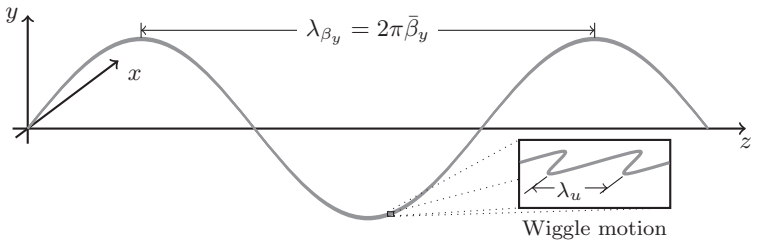

Figure 5.3 Combined motion of the wiggler and betatron oscillations in a planar undulator. The wiggle motion is along $\hat{x}$, while the betatron oscillation has a much longer period along $\hat{y}$.

undulator with flat poles is

$$\boldsymbol{B}(\boldsymbol{x}; z) = -B_0 \cosh(k_u y) \sin(k_u z)\hat{y} - B_0 \sinh(k_u y) \cos(k_u z)\hat{z}. \tag{5.17}$$

This reduces to Eq (5.13) when $y = 0$, while the $\hat{z}$-component of $\boldsymbol{B}$ accounts for the fringe field shown in Fig. 5.4(a). The Lorentz force on an electron due to the 3D undulator field is given by

$$-e[\boldsymbol{v} \times \boldsymbol{B}] = -e \begin{bmatrix} B_z \dfrac{dy}{dt} - B_y \dfrac{dz}{dt} \\ -B_z \dfrac{dx}{dt} \\ B_y \dfrac{dx}{dt} \end{bmatrix} = \frac{d}{dt} \begin{bmatrix} \gamma m \dfrac{dx}{dt} \\ \gamma m \dfrac{dy}{dt} \\ \gamma m \dfrac{dz}{dt} \end{bmatrix}. \tag{5.18}$$

The velocity along x can be determined if we notice from (5.17) that

$$-e\left(B_z \frac{dy}{dt} - B_y \frac{dz}{dt}\right) = \frac{eB_0}{k_u} \frac{d}{dt} \left[\cosh(k_u y) \cos(k_u z)\right]. \tag{5.19}$$

Thus, the $\hat{x}$-component of (5.18) can be directly integrated, and we find that

$$x' \equiv \frac{dx}{dz} = \frac{dx/dt}{dz/dt} \approx \frac{K}{\gamma} \cosh(k_u y) \cos(k_u z) + x'(0), \tag{5.20}$$

where we approximate $dz/dt \approx c$. This result follows simply from the Hamiltonian formalism of Appendix A, for which (5.20) is a consequence of the conservation of canonical momentum along $\hat{x}$. Furthermore, we see that (5.20) yields similar wiggle motion to the 1D result (5.14), only now the oscillation amplitude depends slowly on the y coordinate. Inserting the velocity (5.20) into the $\hat{y}$-component of the Lorentz force (5.18) and neglecting the slow and small time dependence of γ, we find that the motion in the vertical plane is governed by

$$\begin{aligned} y'' &\approx -\frac{K^2 k_u}{\gamma_r^2} \cos^2(k_u z) \sinh(k_u y) \cosh(k_u y) \\ &\approx -\left(\frac{K k_u}{\gamma_r}\right)^2 \cos^2(k_u z) y \end{aligned} \tag{5.21}$$

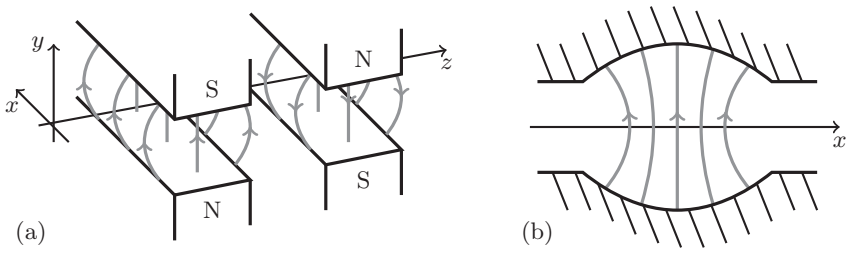

Figure 5.4 (a) The fringe magnetic field of a flat face planar undulator that gives rise to natural focusing. (b) Illustration of a parabolic-pole faced undulator that focuses the beam in both directions.

to first order in $k_u y$. After averaging over an undulator period, this leads to the harmonic oscillator equation

$$y'' = -k_{n0}^2 y, \quad \text{with} \quad k_{n0} = \frac{K k_u}{\sqrt{2}\gamma} \equiv \frac{1}{\beta_n}. \tag{5.22}$$

We see that there is a restorative force along y, so that in the vertical plane the beam's natural beta function β_n is given by the inverse of the oscillation frequency k_{n0}. The natural focusing action in y (but not x) could have been anticipated by realizing that the fast oscillations lead to an average (ponderomotive) force that pushes particles towards regions of lower field strength.

Natural focusing in both planes can be achieved by designing the magnitude of the magnetic field to be a minimum on axis. For example, one can shape the undulator pole faces to have a parabolic profile [4] as shown in Fig. 5.4(b), in which case the magnetic field is

$$\begin{aligned} \boldsymbol{B} = -\frac{B_0}{k_y}\big[& k_x \sinh(k_x x)\sinh(k_y y)\sin(k_u z)\hat{x} \\ & + k_y \cosh(k_x x)\cosh(k_y y)\sin(k_u z)\hat{y} \\ & + k_u \cosh(k_x x)\sinh(k_y y)\cos(k_u z)\hat{z}\big], \end{aligned} \tag{5.23}$$

with $k_x^2 + k_y^2 = k_u^2$ to satisfy Maxwell's equations in vacuum. The field (5.23) leads to natural focusing in both directions, and it can be shown that the natural focusing strength in the x and y planes satisfy $k_{nx}^2 + k_{ny}^2 = k_{n0}^2$.

To summarize, the transverse motion in a planar undulator is given by

$$x = x_w + x_\beta \qquad\qquad y = y_\beta \tag{5.24}$$

with the wiggle motion x_w given by integrating the velocity equations in the wiggler (5.20), and the betatron motion $\boldsymbol{x}_\beta$ is given by

$$x_\beta = x_0 \cos(k_{nx} z) + \frac{x_0'}{k_{nx}} \sin(k_{nx} z) \tag{5.25a}$$

$$y_\beta = y_0 \cos(k_{ny} z) + \frac{y_0'}{k_{ny}} \sin(k_{ny} z). \tag{5.25b}$$

Here, the value of the natural undulator focusing k_n depends on the pole shape, with $k_{nx}^2 + k_{ny}^2 = k_{n0}^2$. The simple harmonic motion in the transverse direction conserves the action $\mathcal{J}_y = (p_y^2 + k_{ny}^2 y^2)/2k_{ny}$ as the electron executes circular motion in the phase space $(k_{n0}y, p_y) = (k_{n0}y, y')$. If the poles are shaped the invariant $\mathcal{J}_x$ can be constructed in an analogous manner; in either case the motion conserves $k_{nx}\mathcal{J}_x$, whose limit is $p_x^2/2$ for $k_{nx} \to 0$.

While the evolution of the transverse degrees of freedom is largely independent of the longitudinal ones, the equation of motion for the ponderomotive phase does depend upon $\boldsymbol{p}$. This coupling arises because particles of equal energies but different transverse momenta have different longitudinal velocities, which results in a spread of θ due to the variation in the resonance condition. To be explicit, we consider the average longitudinal velocity scaled by c:

$$\frac{\bar{v}_z}{c} = \sqrt{1 - \overline{\boldsymbol{x}'^2} - \frac{1}{\gamma^2}} \approx 1 - \frac{1}{2}\left(\overline{x'^2 + y'^2} + \frac{1}{\gamma^2}\right). \tag{5.26}$$

For a planar undulator with flat poles, (5.20) expresses both the wiggle motion and slow drift along $\hat{x}$, while (5.22) describes the simple harmonic motion in $\hat{y}$. Averaging over an undulator period, we have

$$\begin{aligned}
\overline{x'^2 + y'^2} &= \frac{K^2}{2\gamma^2}\cosh^2(k_u y) + x'(0)^2 + y'(z)^2 \\
&\approx \frac{K^2}{2\gamma^2}(1 + k_u^2 y^2) + x'(0)^2 + y'(z)^2 \\
&= \frac{K^2}{2\gamma^2} + 2\left(k_{n,x}\mathcal{J}_x + k_{n,y}\mathcal{J}_y\right),
\end{aligned} \tag{5.27}$$

where we have expressed the angular spread in terms of the actions $\mathcal{J}_{x,y}$, so that (5.27) is valid for arbitrary pole shape. Thus, natural undulator focusing preserves the average longitudinal velocity for each electron. To see why this is so, consider the betatron motion along y shown in Fig. 5.3: y' is maximum on axis while zero at maximum y. The magnetic field at this turning point is larger than that on axis, resulting in wiggle oscillations along x that have a larger amplitude. As shown in (5.27), these two effects compensate each other, so that $\overline{x'^2 + y'^2}$ and, hence, $\bar{v}_z$, is constant. Thus, we have

$$\frac{\bar{v}_z}{c} = 1 - \frac{1 + K^2}{2\gamma^2} - \frac{\boldsymbol{p}^2 + k_\beta^2 \boldsymbol{x}^2}{2} = 1 - \frac{1 + K^2}{2\gamma^2} - \left(k_{n,x}\mathcal{J}_x + k_{n,y}\mathcal{J}_y\right). \tag{5.28}$$

The values of $\mathcal{J}_x$ and $\mathcal{J}_y$ depend on the initial conditions $(\boldsymbol{x}(0), \boldsymbol{p}(0))$, which in turn vary from electron to electron. Along any particular particle trajectory, however, $\mathcal{J}_{x,y}$ are conserved. If we initialize the transverse electron distribution function to be constant along lines of fixed $\mathcal{J}$ (i.e., distribute the particles uniformly in the phase conjugate to $\mathcal{J}$), than the resulting matched beam envelope is invariant along the undulator as we show in Fig. (5.5). For a beam of emittance

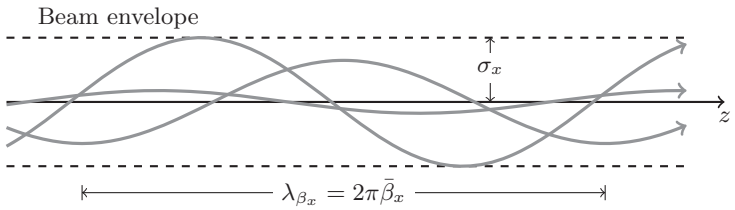

Figure 5.5 Matched beam in a undulator focusing channel.

ε_x, the matched rms beam size is

$$\sigma_y \sim \sqrt{\frac{\varepsilon_x \gamma_r \lambda_u}{2\pi K}} = \sqrt{\frac{\varepsilon_{x,n} \lambda_u}{2\pi K}}. \tag{5.29}$$

The matched beam size (5.29) is typically much larger than the optimal beam size $\sigma_{\rm opt} \sim \sqrt{\lambda_1 L_G/4\pi}$, especially at x-ray wavelengths; for example, if $\varepsilon_x = \lambda_1/4\pi$, than $\sigma_y/\sigma_{\rm opt} \approx \sqrt{K/2\rho} \gg 1$. Thus, high-gain x-ray FELs require additional focusing provided by external magnets.

5.2.2 Betatron Motion in an External Focusing Lattice

As we saw in the previous section, the natural focusing strength $k_{n0} \propto \gamma^{-1}$ is typically too weak to produce a sufficiently small matched beam size, especially for short wavelength FELs that use high energy electron beams. To further reduce the cross sectional area, x-ray FELs usually incorporate alternating-gradient focusing such as that provided by a FODO lattice. We discussed stable beam propagation in a FODO lattice in Sec. 1.1.4, concentrating on a focusing lattice designed to maintain a nearly constant beam size and divergence. While the full FODO dynamics can be easily incorporated into numerical simulations, we will make some additional approximations in order to gain further analytic understanding regarding the effects of finite beam size, divergence, and emittance on the FEL performance.

Our discussion of the single particle transverse dynamics requires a few additional concepts used in accelerator physics. As implied by the fact that the linear dynamics is governed by a second order differential equation, linear particle optics can be mapped to a generalized simple harmonic oscillator, with natural coordinates given by the particle amplitude and phase in both transverse directions. In accelerator terminology, the transverse degrees of freedom can be written in terms of the Courant-Snyder (Twiss) lattice functions $\beta_{\boldsymbol{x}}$ and $\alpha_{\boldsymbol{x}}$ as

$$\boldsymbol{x}_\beta(z) = \sqrt{2\mathcal{J}_{\boldsymbol{x}}\beta_{\boldsymbol{x}}(z)}\cos\Phi_{\boldsymbol{x}}(z) \tag{5.30}$$

$$\boldsymbol{p}(z) \equiv \boldsymbol{x}'_\beta(z) = -\sqrt{\frac{2\mathcal{J}_{\boldsymbol{x}}}{\beta_{\boldsymbol{x}}(z)}}\left[\sin\Phi_{\boldsymbol{x}}(z) + \alpha_{\boldsymbol{x}}(z)\cos\Phi_{\boldsymbol{x}}(z)\right], \tag{5.31}$$

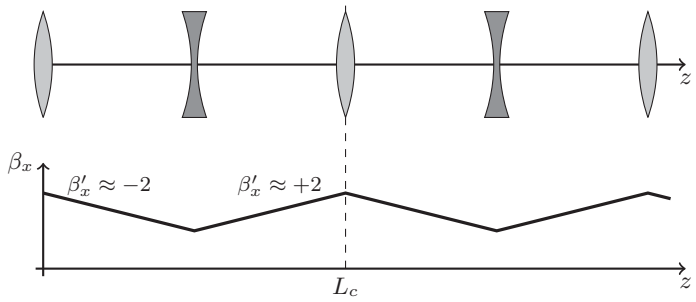

Figure 5.6 Variation of the horizontal beta function along the distance of two FODO cells for a small phase advance per cell. The derivative $\beta_x' \equiv d\beta_x/dz$ is close to the values ± 2, but the deviation of β_x from the average value $\hat{\beta}$ is relatively small. The FODO cell length 2ℓ is assumed to be much smaller than the average beta $\hat{\beta}$.

where the betatron phase advance $\Phi_{\boldsymbol{x}}(z) \equiv \int dz'\, 1/\beta_{\boldsymbol{x}}(z')$ describes the generalized rotation in phase space, $\beta_{\boldsymbol{x}}(z)$ sets the oscillation amplitude, and the actions $\mathcal{J}_x$ and $\mathcal{J}_y$ are (distinct) invariants for each particle determined by the initial conditions. Eq. (5.31) follows from differentiating (5.30) and using the definitions $d\Phi_{\boldsymbol{x}}/dz = 1/\beta_{\boldsymbol{x}}$ and $d\beta_{\boldsymbol{x}}/dz = 2\langle \boldsymbol{x}'\boldsymbol{x}\rangle = -2\alpha_{\boldsymbol{x}}$. From (5.31), we can write the transverse velocity squared of an electron as

$$\begin{aligned} \boldsymbol{p}^2 &= \frac{2\mathcal{J}_{\boldsymbol{x}}}{\beta_{\boldsymbol{x}}(z)} \left\{ \alpha_{\boldsymbol{x}}^2(z) + [1 - \alpha_{\boldsymbol{x}}^2(z)] \sin^2 \Phi_{\boldsymbol{x}}(z) + \alpha_{\boldsymbol{x}}(z) \sin[2\Phi_{\boldsymbol{x}}(z)] \right\} \\ &\approx \frac{2\mathcal{J}_{\boldsymbol{x}}}{\beta_{\boldsymbol{x}}(z)} \left\{ 1 \pm \sin[2\Phi_{\boldsymbol{x}}(z)] \right\}, \end{aligned} \tag{5.32}$$

where the final line results from the fact that the particular FODO lattice used for FELs has $\alpha_{\boldsymbol{x}}(z) \approx \pm 1$ as we showed in (1.33). The beam has positive α_x (negative correlation $\langle xx' \rangle$) in the drift space following the focusing quadrupole, while after the defocusing quad $\alpha_x \approx -1$. Furthermore, since the average beta-function is much greater than the drift length, $\bar{\beta} \gg \ell$, the phase $\Phi_{\boldsymbol{x}}(z)$ changes only a small amount over the drift space, so that we can average the final term to zero if the gain length is much larger than drift space [5]. Thus, we can approximate the angle squared in the transverse degrees of freedom by

$$p_x^2(z) \approx \frac{2\mathcal{J}_x}{\bar{\beta}_x} = \text{constant}, \qquad p_y^2(z) \approx \frac{2\mathcal{J}_y}{\bar{\beta}_y} = \text{constant}. \tag{5.33}$$

Although the $\mathcal{J}_{\boldsymbol{x}}$ are constants of motion for each electron, different electrons generally have different transverse actions. In fact, the ensemble average of $\mathcal{J}_{\boldsymbol{x}}$ over all the electrons is the rms transverse emittance of the beam, i.e.,

$$\langle \mathcal{J}_x \rangle = \varepsilon_x \qquad \langle \mathcal{J}_y \rangle = \varepsilon_y. \tag{5.34}$$

While (5.30)-(5.31) is a complete representation of the transverse motion with (5.33) a reasonably accurate approximation to $\boldsymbol{p}^2$ for most FEL applications,

our subsequent analysis requires a more analytically amenable description of the transverse physics. The model motion should reflect the fact that the rms beam size is nearly constant in the FODO lattice and, more importantly, have a faithful representation of the coupling between the transverse and longitudinal degrees of freedom. While we have seen that the transverse physics is independent of the longitudinal ones, both $\boldsymbol{p}$ and $\boldsymbol{x}$ affect the evolution of the particle phase by changing the mean velocity of the particle. In terms of the approximation (5.33), we have

$$\frac{\bar{v}_z}{c} \approx 1 - \frac{1 + K^2/2}{2\gamma^2} - \frac{\mathcal{J}_x + \mathcal{J}_y}{\bar{\beta}}. \tag{5.35}$$

Thus, our approximate motion should at a minimum respect the following characteristics of the true dynamics in the FODO lattice:

1. Result in a stable beam with nearly constant rms size equal to $\sqrt{\varepsilon_x \bar{\beta}_x}$;
2. Be periodic in z with period given by $\bar{\beta}_x/2\pi = 1/(2\pi k_\beta)$;
3. Possess an invariant whose beam average is proportional to ε_x that can be associated with a decrease in $\bar{v}_z$ similar to (5.35).

All three conditions can be satisfied by approximating the particle trajectories by the simple harmonic motion for smooth focusing that we studied in the previous section. For this reason and for analytic tractability, in what follows we will approximate the effect of the FODO lattice by a smooth focusing field whose focusing strength (oscillator frequency) $k_\beta = 1/\bar{\beta}_x$.

To see how these approximations work in practice, we include Fig. 5.7 that compares some aspects of the single particle dynamics in a FODO lattice with a smooth focusing channel. In Fig. 5.7(a) we plot as a solid line the phase space ellipses at the center of the drift space after both the focusing (top) and defocusing (bottom) quadrupole. We also include dots representing particle positions in each half-section after 0 (0.5), 4 (4.5), 8 (8.5), and 12 (12.5) lattice periods. The FODO parameters are based on the LCLS lattice that has $\bar{\beta}_x \approx 18$ m and $\ell \approx 4$ m. For comparison, we also plot the phase space ellipse for a smooth focusing channel/simple harmonic oscillator (SHO) with $k_\beta = 1/\bar{\beta}_x$ as a dashed line, including particle phase space points at the same z locations. The two show reasonable agreement when averaged over several lattice periods.

In addition, we plot the $\bar{\beta}_x p_x^2/2$ for the FODO lattice, and compare it to the invariant action $\mathcal{J}_x$ of the smooth focusing channel/SHO in Fig. 5.7(b). Note that p_x^2 for the FODO lattice is only truly invariant in the drift section, and that it oscillates about the mean value given by $\mathcal{J}_x$. Thus, the single-particle transverse coupling to θ provided by the smooth focusing lattice only matches that of a FODO lattice when averaged over many focusing cells. Furthermore, the difference from the mean changes sign every half period such that $\bar{\beta}_x p_x^2/2$ averaged over any full period approximately equals the action $\mathcal{J}_x$.

As shown in Fig. 5.7, the particle trajectories in the smooth focusing channel only roughly mimic those of the FODO lattice. Nevertheless, in the next few

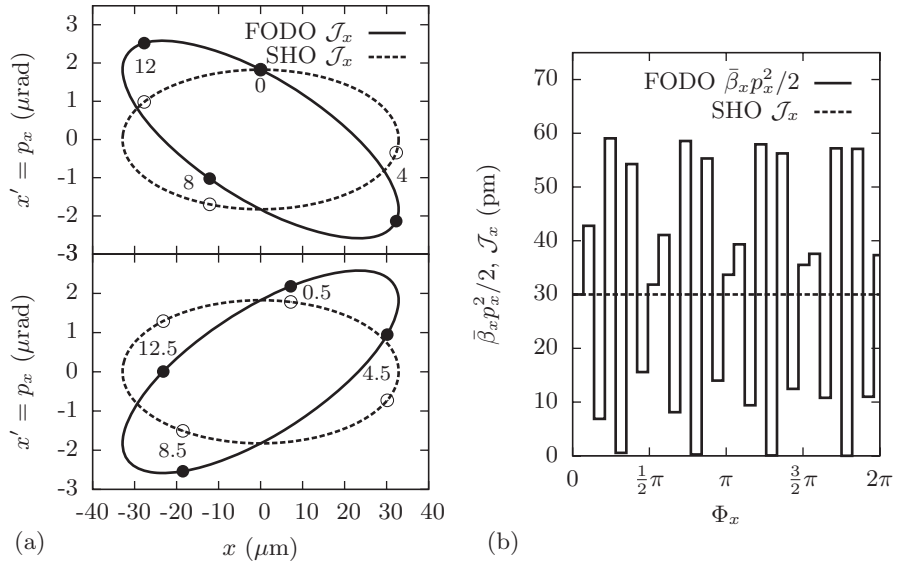

Figure 5.7 Comparison between the particle motion in a FODO lattice and a constant focusing channel (simple harmonic oscillator/SHO). The solid line ellipses in panel (a) are equal-action contours drawn at the center of the each drift space, with the top being just after the focusing quad, and the bottom just after the defocusing quad. The dotted lines are equal action lines for the constant focusing lattice (simple harmonic oscilaltor/SHO). Filled and unfilled dots represent one single particle position plotted every four FODO periods. Panel (b) plots the particle $\bar{\beta}_x p_x^2/2$ in the FODO lattice as a solid line, whose average (dashed line) equals $\mathcal{J}_x = (\beta_x p_x^2 + x^2/\beta_x)/2$ for the constant focusing channel/SHO.

sections we will present analysis based upon this approximate motion that results in rather accurate semi-analytic predictions regarding the FEL gain and mode shape. This is because these radiation characteristics do not depend directly on the individual particle orbits, but rather on certain averaged properties of the particle beam distribution. Since the low-order moments of a beam in a FODO lattice are accurately represented by an ensemble of electrons moving in a smooth focusing channel, they yield remarkably accurate predictions for the FEL performance. The matched beam size (as shown in Fig. 5.5) and divergence are given in terms of the emittance ε_x as

$$\sigma_x = \sqrt{\frac{\varepsilon_x}{k_{\beta,x}}}, \quad \sigma_{x'} = \sqrt{\varepsilon_x k_{\beta,x}}. \tag{5.36}$$

The equations for the matched beam and coupling to θ in a FODO lattice are identical in form to those describing the natural focusing that we derived in the previous Section. Thus, the smooth focusing approximation for the 3D FEL equations of motion can be used in either setting provided that the focusing

strength $k_\beta = 1/\bar{\beta}$ is appropriately interpreted. We now turn to completing the derivation of the FEL equations in 3D.

5.3 3D Equations of the FEL

In this section, we derive 3D governing equations for an FEL. Our goal is to obtain the coupled Maxwell-Klimontovich system for the radiation and electron beam. The radiation field will be governed by the paraxial wave equation driven by an appropriately defined FEL current, while the characteristic curves of the Klimontovich equation are given by the single particle equations in 3D. These particle equations generalize the 1D FEL pendulum equations to include transverse effects.

5.3.1 Field equation

The derivation of the paraxial wave equation is a straightforward 3D generalization of the 1D arguments laid out in Ch. 3. The full Maxwell equation for the transverse electric field is

$$\left[\frac{1}{c^2}\frac{\partial^2}{\partial t^2} - \frac{\partial^2}{\partial z^2} - \boldsymbol{\nabla}_\perp^2\right] E_x = -\frac{1}{\epsilon_0 c^2}\left[\frac{\partial J_x}{\partial t} + c^2\frac{\partial \rho_e}{\partial x}\right], \tag{5.37}$$

where $\boldsymbol{\nabla}_\perp^2$ is the transverse Laplacian, ρ_e is the electron charge density, and the three-dimensional current density is

$$J_x = -ecK\cos(k_u z)\sum_{j=1}^{N_e}\frac{1}{\gamma_j}\delta[z - z_j(t)]\delta[\boldsymbol{x} - \boldsymbol{x}_j(t)]. \tag{5.38}$$

FELs are characterized by

$$J_x \sim v_x\rho_e \sim \frac{cK}{\gamma}\rho_e \qquad\qquad \frac{\partial}{\partial t} \sim \omega_1 \sim \frac{2\pi c}{\lambda_1} \tag{5.39}$$

and

$$\frac{\partial}{\partial x} \sim \frac{1}{\sigma_x} \sim \frac{1}{\sqrt{\lambda_1\lambda_u}}\begin{cases}\sqrt{1/N_u} & \text{in the low gain regime}\\ 4\pi\sqrt{\rho} & \text{in the high gain regime.}\end{cases} \tag{5.40}$$

Thus, for $K > 1$ the ratio of the charge to current source is small:

$$\frac{c^2\partial\rho_e/\partial x}{\partial J_x/\partial t} \sim \frac{1}{2\pi}\begin{cases}\sqrt{1/N_u} & \text{in the low gain regime}\\ 4\pi\sqrt{\rho} & \text{in the high gain regime.}\end{cases} \tag{5.41}$$

Additionally, the charge density term does not resonantly drive the field at lowest order. In fact, it can be shown that the slowly varying part of ρ_e comes in with another transverse derivative, so that the resonant coupling to the charge density is actually $O(\rho)$ [or $O(1/N_u)$] smaller than that to the current density J_x. Thus, we can drop the charge density term from the Maxwell equation.

We again introduce the Fourier transform of the field envelope centered at the normalized frequency $\nu = \omega/\omega_1$

$$\begin{aligned} E_x &= \tilde{E}(\boldsymbol{x}, t; z) e^{ik_1(z-ct)} + c.c. \\ &= \int d\nu \; e^{i\nu k_1(z-ct)} E_\nu(\boldsymbol{x}; z) e^{i\Delta\nu k_u z} + c.c. \end{aligned} \tag{5.42}$$

and make the slowly-varying phase and envelope approximation, assuming that $|\partial E_\nu/\partial z| \ll k_1 |E_\nu|$. The derivation proceeds exactly as the 1D analysis done in Sec. 3.4, with the transverse Laplacian now along for the ride: we drop second order z derivatives, introduce the slowly varying ponderomotive particle phase

$$\begin{aligned} \theta_j(z) &\equiv (k_u + k_1)z - ck_1 \bar{t}_j(z) \\ &\equiv (k_u + k_1)z - ck_1 \left[t_j(z) - \frac{K^2}{ck_1(4+2K^2)} \sin(2k_u z) \right], \end{aligned} \tag{5.43}$$

and average the equation over an undulator period. The resulting paraxial wave equation for the slowly varying amplitude $E_\nu(\boldsymbol{x}; z)$ is

$$\left(\frac{\partial}{\partial z} + i\Delta\nu k_u + \frac{\boldsymbol{\nabla}_\perp^2}{2ik_1} \right) E_\nu(\boldsymbol{x}; z) = -\kappa_1 \frac{k_1}{2\pi} \sum_{j=1}^{N_e} e^{-i\nu\theta_j(z)} \delta[\boldsymbol{x} - \boldsymbol{x}_j(z)], \tag{5.44}$$

where we recall that the normalized frequency difference $\Delta\nu \equiv \nu - 1$ and the coupling $\kappa_1 \equiv eK[\mathrm{JJ}]/4\epsilon_0\gamma_r$. Note that we approximate $1/k$ by $1/k_1$ in the transverse derivatives, as the difference between these is assumed small. Additionally, it is easy to verify that the field equation above is related to the undulator paraxial equation (2.58) by the transverse Fourier transform, with the added generalization that the initial electron phase $\omega_1 t_j(0)$ relevant to spontaneous emission is replaced in the FEL with the dynamical ponderomotive phase $-\theta_j(z)$.

5.3.2 Electron equations of motion

Most of the heavy lifting required to derive the single particle equations of motion has already been done, partly in the 1D analysis of Sec. 3.2 and partly when we discussed the transverse degrees of freedom earlier in this Chapter. Here, we review some of the salient points and collect the final 3D equations.

The rate of work done on the electrons by the radiation is given by $\boldsymbol{F} \cdot \boldsymbol{v}$, which for the FEL equals the product of the undulator wiggle velocity along $\hat{x}$ and the transverse electric field. Changing the independent variable from $t \to z$, we have

$$\begin{aligned} mc^2 \frac{d\gamma}{dz} &= -e \frac{dx}{dz} E_x \\ &= \frac{eK}{\gamma} \cos(k_u z) \left[\int d\nu \; E_\nu(\boldsymbol{x}; z) e^{i\nu(k_1 z - \omega_1 t)} e^{i\Delta\nu k_u z} + c.c. \right]. \end{aligned} \tag{5.45}$$

Replacing the Lorentz factor with the normalized energy deviation from resonance $\eta \equiv (\gamma - \gamma_r)/\gamma_r$, and the particle time with θ using (5.43), we average over

the fast oscillations in the undulator to obtain

$$\frac{d\eta}{dz} = \chi_1 \int d\nu \; E_\nu(\boldsymbol{x}; z) e^{i\nu\theta} + c.c. \tag{5.46}$$

where again $\chi_1 \equiv eK[\mathrm{JJ}]/(2\gamma_r^2 mc^2)$.

To determine the rate of change of the ponderomotive phase, we differentiate (5.43)

$$\frac{d\theta}{dz} = (k_u + k_1) - k_1 \frac{c}{\bar{v}_z}, \tag{5.47}$$

where $\bar{v}_z$ is the mean particle velocity averaged over an undulator period. The particle is slowed from its maximum longitudinal speed $\sqrt{1 - 1/\gamma^2}$ due to the transverse motion, which now includes both an average of the fast wiggle oscillation in the undulator field and the slow betatron dynamics given by (5.25):

$$\frac{c}{\bar{v}_z} \approx 1 + \frac{1}{2\gamma^2} + \frac{\overline{x'^2 + y'^2}}{2} \approx 1 + \frac{1 + K^2/2}{2\gamma_r^2}(1 - 2\eta) + k_{\beta,x}\mathcal{J}_x + k_{\beta,y}\mathcal{J}_y, \tag{5.48}$$

where the focusing strength k_β is determined by either the natural undulator focusing or by the external FODO lattice if the latter is much stronger. The first two constant terms in (5.48) cancel the $(k_u + k_1)$ in the phase equations (5.47) due to the resonance condition, leaving only the deviations from the ideal on-resonance, on-axis trajectory in the phase evolution

$$\frac{d\theta}{dz} = 2k_u\eta - \frac{k_1}{2}\left(\boldsymbol{p}^2 + k_\beta^2 \boldsymbol{x}^2\right) \tag{5.49}$$

$$= 2k_u\eta - k_1 k_\beta \mathcal{J} = 2k_u\eta - k_1 H_\perp. \tag{5.50}$$

Here, the focusing k_β is the inverse of the average betatron function $\bar{\beta}_{x,y}$, and we use the smooth focusing approximation to characterize the transverse betatron oscillation, in which case $(\boldsymbol{p}^2 + k_\beta^2 \boldsymbol{x}^2)/2 = k_\beta \mathcal{J} = H_\perp$ is a constant of motion. The transverse degrees of freedom therefore obey

$$\frac{d\boldsymbol{x}}{dz} = \boldsymbol{p} \qquad\qquad \frac{d\boldsymbol{p}}{dz} = -k_\beta^2 \boldsymbol{x}. \tag{5.51}$$

Collecting the 3D particle equations for convenience, we have

$$\frac{d\theta}{dz} = 2k_u\eta - \frac{k_1}{2}(\boldsymbol{p}^2 + k_\beta^2 \boldsymbol{x}^2), \tag{5.52}$$

$$\frac{d\eta}{dz} = \chi_1 \int d\nu \; e^{i\nu\theta} E_\nu(\boldsymbol{x}; z) + c.c., \tag{5.53}$$

$$\frac{d\boldsymbol{x}}{dz} = \boldsymbol{p}, \qquad\qquad \frac{d\boldsymbol{p}}{dz} = -k_\beta^2 \boldsymbol{x}, \tag{5.54}$$

where $\chi_1 = eK[\mathrm{JJ}]/(2\gamma_r^2 mc^2)$.

5.3.3 Coupled Maxwell-Klimontovich Equations

We describe the electrons with their microscopic distribution in phase space. In a manner similar to the 1D analysis, we define the electron Klimontovich

distribution function

$$F(\theta,\eta,\boldsymbol{x},\boldsymbol{p};z)=\frac{k_1}{n_e}\sum_{j=1}^{N_e}\delta[\theta-\theta_j(z)]\delta[\eta-\eta_j(z)] \times\delta[\boldsymbol{x}-\boldsymbol{x}_j(z)]\delta[\boldsymbol{p}-\boldsymbol{p}_j(z)], \tag{5.55}$$

where n_e is the peak electron volume density. Note that integrating (5.55) over $\boldsymbol{p}$ and setting $\delta(\boldsymbol{x}-\boldsymbol{x}_j)\to 1/(2\pi\sigma_x^2)$ yields the 1D F defined in (4.8). The evolution of the Klimontovich distribution function is governed by the continuity equation

$$\frac{\partial F}{\partial z}+\frac{d\theta}{dz}\frac{\partial F}{\partial\theta}+\frac{d\eta}{dz}\frac{\partial F}{\partial\eta}+\frac{d\boldsymbol{x}}{dz}\cdot\frac{\partial F}{\partial\boldsymbol{x}}+\frac{d\boldsymbol{p}}{dz}\cdot\frac{\partial F}{\partial\boldsymbol{p}}=0, \tag{5.56}$$

with the equations of motion given by Eqs. (5.52), (5.53), and (5.54).

The rest of this chapter will be devoted to analyzing the 3D FEL equations in the small signal regime, applicable for linear FEL gain before saturation. To do this, we again divide the distribution function F into a smooth background $\bar{F}$ that is independent of θ and a fluctuation δF that describes the θ-scale variations. This δF contains the particle shot noise and the FEL-generated micro-bunching, while assuming $\bar{F}$ to be uniform in θ (the coasting beam approximation) is valid if the e-beam current, energy spread, emittance, etc. is nearly constant over a coherence length. Using the decomposition $F=\bar{F}+\delta F$, we Fourier transform (5.56) and neglect the higher-order terms $\sim E_\nu F_\nu$ to obtain the following linear system

$$\left\{\frac{\partial}{\partial z}+\boldsymbol{p}\cdot\frac{\partial}{\partial\boldsymbol{x}}-k_\beta^2\boldsymbol{x}\cdot\frac{\partial}{\partial\boldsymbol{p}} +i\nu\left[2\eta k_u-\frac{k_1}{2}(\boldsymbol{p}^2+k_\beta^2\boldsymbol{x}^2)\right]\right\}F_\nu=-\chi_1 E_\nu\frac{\partial}{\partial\eta}\bar{F} \tag{5.57}$$

$$\left\{\frac{\partial}{\partial z}+\boldsymbol{p}\cdot\frac{\partial}{\partial\boldsymbol{x}}-k_\beta^2\boldsymbol{x}\cdot\frac{\partial}{\partial\boldsymbol{p}}\right\}\bar{F}=0, \tag{5.58}$$

where F_ν is the Fourier transform of δF, which we assume is localized about the one of the odd harmonic resonant frequencies $\nu\approx h$ (typically we take $h=1$). The linear system (5.57)-(5.58) applies before saturation when the optical power $P\ll\rho P_{\rm beam}$.

A significant difference between the 3D equation (5.58) and its 1D counterpart is the fact that the background distribution $\bar{F}$ now has non-trivial z-dependence due to the transverse degrees of freedom. To solve for $\bar{F}(\boldsymbol{x},\boldsymbol{p};z)$, we integrate along the transverse particle trajectories, which are the characteristic curves of (5.58). The physics of this solution was discussed in Sec. 1.1.5: the value of $\bar{F}$ is transported along the single particle trajectories, so that [6]

$$\bar{F}(\boldsymbol{x},\boldsymbol{p};z)=\bar{F}[\boldsymbol{x}_0(\boldsymbol{x},\boldsymbol{p},z;0),\boldsymbol{p}_0(\boldsymbol{x},\boldsymbol{p},z;0);0]. \tag{5.59}$$

Here, the initial coordinates $(\boldsymbol{x}_0,\boldsymbol{p}_0)$ are functions of the present coordinates

$(\boldsymbol{x}, \boldsymbol{p})$ and z that satisfy the transverse equations of motion subject to the initial conditions $(\boldsymbol{x}_0, \boldsymbol{p}_0) = (\boldsymbol{x}, \boldsymbol{p})$ at $z = 0$. For an arbitrary initial point s, the trajectories in the smooth focusing lattice are

$$\boldsymbol{x}_0(\boldsymbol{x}, \boldsymbol{p}, z; s) = \boldsymbol{x} \cos[k_\beta(z-s)] - \frac{\boldsymbol{p}}{k_\beta} \sin[k_\beta(z-s)] \tag{5.60}$$

$$\boldsymbol{p}_0(\boldsymbol{x}, \boldsymbol{p}, z; s) = \boldsymbol{p} \cos[k_\beta(z-s)] + k_\beta \boldsymbol{x} \sin[k_\beta(z-s)]. \tag{5.61}$$

Having solved for $\bar{F}$ at lowest order, we conclude this section by collecting the linearized equations for the field E_ν and density perturbation F_ν. We insert the definition of the electron distribution function into the paraxial wave equation (5.44), include the Liouville equation Eq. (5.57), and extend both to harmonic interaction to find that the linear Maxwell-Klimontovich equations for the FEL in 3D are

$$\left(\frac{\partial}{\partial z} + i\Delta\nu k_u + \frac{\boldsymbol{\nabla}_\perp^2}{2ik} \right) E_\nu = -\kappa_h n_e \int d\boldsymbol{p} d\eta \; F_\nu \tag{5.62}$$

$$\begin{aligned} \left\{ \frac{\partial}{\partial z} + \boldsymbol{p} \cdot \frac{\partial}{\partial \boldsymbol{x}} - k_\beta^2 \boldsymbol{x} \cdot \frac{\partial}{\partial \boldsymbol{p}} \right. \\ \left. + i \left[2\nu\eta k_u - \frac{k}{2}(\boldsymbol{p}^2 + k_\beta^2 \boldsymbol{x}^2) \right] \right\} F_\nu = -\chi_h E_\nu \frac{\partial}{\partial \eta} \bar{F}. \end{aligned} \tag{5.63}$$

We will solve the linear FEL equations (5.62)-(5.63) with $\bar{F}$ given by (5.59) in both the low-gain and high-gain regimes using two different mathematical techniques. The low-gain solution will be obtained by integrating over the unperturbed trajectories/characteristics of δF and E_ν, namely, those ignoring the coupling between the distribution function and the electromagnetic field. This solution will be valid if the E_ν does not change significantly during its interaction with the undulator, meaning that this solution will generalize the 1D low-gain results of Sec. 3.3 and Sec. 4.2.

The high gain analysis will more closely resemble that of Sec. 3.4, and will focus on understanding the 3D FEL solution with the largest growth rate. While this method could in principle include the low-gain results as a special case, we will simplify the discussion by restricting our attention to only the growing modes.

5.4 Solution in the Low-Gain Regime

In this section we derive a formula for the linear gain including the effects of beam emittance and energy spread when the external focusing can be approximated by the constant focusing parameter k_β. This derivation follows that of Ref. [6], and is a 3D generalization of the 1D analysis in Sec. 4.2 that solves the low-gain FEL equations by integrating along the transverse particle trajectories (characteristic curves). To consolidate notation, we abbreviate the transverse phase space coordinates as $\boldsymbol{Z} \equiv (\boldsymbol{x}, \boldsymbol{p})$, in which case the derivatives on the left-hand-side of the